Sensor radiance physical model for rugged heterogeneous surfaces in the 3-14 μm region

S. Pallotta, X. Briottet, C. Miesch, Yann H. Kerr

Sensor radiance physical model for rugged heterogeneous surfaces in the 3-14 µm region.

Sandrine Pallotta, Xavier Briottet and Christophe Miesch

Département d'Optique Théorique et Appliquée, Office National d'Etudes et de Recherches Aérospatiales, BP 4025, 31055 Toulouse France
Sandrine.Pallotta@onecert.fr , Xavier.Briottet@onecert.fr , Christophe.Miesch@onecert.fr

Yann Kerr

Centre d'Etude Spatial de la BIOsphère, 18 avenue E. Belin, bpi 2801, 31401 Toulouse cedex 9 France
Yann.kerr@cesbio.cnes.fr

Abstract: We present a physical model describing the radiance acquired by an infrared sensor over a rugged heterogeneous surface. This model predicts the radiance seen over complex landscapes like urban areas and provides an accurate analysis of the signal, as each component is available at ground and sensor level. Plus, it allows data comparison from different instruments. Two representative cases (natural and urban) are analysed to show the composition and the construction of the sensor signal and to highlight the importance of having a 3D model, especially for rugged surfaces where environment weights in the overall spectral domain.

OCIS codes: (120.0280) Remote Sensing; (120.5700) Reflectance; (120.6660) Surface measurements, roughness.

References and links

1. D. Llewellyn-Jones, M. C. Edwards, C. T. Mutlow, A. R. Birks, I. J. Barton and H. Tait, "AATSR: global-change and surface-temperature measurements from ENVISAT," ESA bulletin (ISSN 0376-4265) **105**, 11-21 (2001).
2. A. Monti Guarnieri, D. Daria, C. Cafforio, P.Guccione, P. Pasquali, D. Nüetsch, D. Small, E. Meier and Y. L. Desnos, "ENVISAT interferometry for mapping and monitoring: preliminary results," in *Proceedings of the FRINGE 2003 workshop (ESA SP – 550)*, ESA /ESRIN, Italy, 1-5 December 2003.
3. J. Okkonen, T. Hyvarinen and E. Herrala, "AISA Airborne Imaging Spectrometer–on its way from hyperspectral research to operative use," in *International airborne remote sensing conference and exhibition – Development, integration, applications and operations, 3rd*, Copenhagen, Denmark,1997; United States, July 7-10 1997, pp I-189- I-196.7
4. ONERA, Timbre-Poste : http://www.onera.fr/visiononera/2005-02/faits-marquants.html#3 .
5. K. D. Bishop and M. J. Diestel, "Airborne remote earth sensing program: an operational airborne MWIR imaging spectrometer and applications," in *Hyperspectral Remote Sensing and Applications*, S. S. Shen, ed., Proc. SPIE 2821, 183-194 (1996).
6. J. A Voogt and T. R. Oke, "Thermal remote sensing of urban climates," Remote Sens. Environ. **86**, 370-384 (2003).
7. V. Masson, G. Pigeon, P. Durand, L. Gomes, J. Salmond, J. P. Lagouarde, J. Voogt, T. R. Oke and C. Lac, "The canopy and aerosol particles interaction in Toulouse urban layer (CAPITOUL) experiment: first results," in *Proceedings Fifth Symposium on the Urban Environment, AM*S, 2004.
8. J. P. Lagouarde, P. Moreau, M. Irvine, J. M. Bonnefond, J. A. Voogt and F. Solliec, "Airborne experimental measurements of the angular variations in surface temperature over urban areas : case study of Marseille (France)," Remote. Sens. Environ. **93**, 443-462 (2004).
9. A. Berk, G. P. Anderson, P. K. Acharya, J. H. Chetwynd, L. S. Bernstein, E. P. Shettle, M. W. Matthew and S. M. Adler-Golden, "Modtran4," (1999).
10. C. Miesch, L. Poutier, V. Achard, X. Briottet, X. Lenot and Y. Boucher, "Direct and inverse radiative transfer solutions for visible and near-infrared hyperspectral imagery," IEEE Trans. Geosci. Remote Sens. **43**, 1552-1562 (2005).
11. P. Guillevic, "Modélisation des bilans radiatifs et énergétiques des couverts végétaux," M. S. thesis (P. Sabatier University, 1999).

#8507 - $15.00 USD Received 18 August 2005; revised 27 February 2006; accepted 3 March 2006

12. NASA/JHU, ASTER thermo-optical database, http://www.jpl.nasa.gov/ .
13. A. Malaplate, F. Nerry, M. P. Stoll, B. Guillame and X. Briottet, "Combined field [3-5µm] and [8-14µm] infrared imaging: approaches to extracting target's bi-directional reflectivity and emissivity,".in 8st Inter. Symposium on remote sensing, SPIE-EOS-NASA-CNES, Sept. 17-21, Toulouse, France 2001.

1. Introduction

Surface temperature is a key parameter in the study of natural surfaces because it results directly from the surface energy balance. In the case of terrestrial surface, infrared remote sensing measurements probably represent the best practical mean for observing surface temperature. However, the use of Thermal InfraRed (TIR) satellite data still induces many methodological and measurement problems, such as:

- Directional effects must be more accurately known both to evaluate the bias they introduce in the measurements and to use the information they contain;
- A good understanding of the effects induced by soil heterogeneity is required for scale change: from field or local scale (e.g. ground measurements) to regional or global scale (e.g. airborne or satellite measurements);
- The quality of sensible heat flux estimates depends on how well relations between radiative and aerodynamic temperatures on heterogeneous surfaces are known; actually the turbulent flux equations require the aerodynamic temperature, not the radiative temperature which is the one accessible by remote sensing.

Furthermore, when the observed surface is heterogeneous, the global surface temperature has a directional character. Though the interest in multidirectional TIR measurements is increasing with the access of data from the Advanced Along Track Scanning Radiometer (AATSR) instrument [1], aboard the ENVIronment SATellite (ENVISAT) [2], the impact of the heterogeneities on this temperature and especially on the signal measured, i.e. directional radiance, is still under study. Furthermore, using new thermal infrared airborne sensors with a high spatial resolution (like AISA [3], Timbre-Poste [4], ARES [5],), it becomes possible to improve research on urban area to understand the impact of the urban heat island on the climatology (Voogt and Oke [6], Masson et al [7], Lagouarde et al [8]). For these metric spatial resolutions, it is necessary to take into account the 3D geometry of such landscape.

Hence, in order to understand the sensor signal acquired in different viewing conditions over an heterogeneous landscape, a radiative transfer code able to compute radiance at sensor level taking into account this heterogeneity is required. In this context, our objective is the development of such a radiative transfer model for complex heterogeneous surfaces (in particular with relief) for a radiance signal measured by an infrared instrument. Until now, this question was not studied in detail, except for homogeneous surfaces. For instance, Modtran [9] considers only flat and homogeneous landscape. Recently, a new code, Comanche [10], based on Modtran kernel, is able to estimate sensor radiance from a flat but heterogeneous ground scene, with its bidirectional reflectance effects. Trapping and environmental atmospheric phenomena are also considered in the reflective domain. However, most terrestrial scenes are not flat and as roughness significantly modifies the signal behaviour, 3D radiative transfer is required. First 3D codes appear like TDART [11] but they are not suited for our objective since they do not allow an accurate term by term analysis of all the contributors of the signal.

Our work aims to present (§2) a new radiative transfer code in the Earth atmosphere system, allowing to model all the radiances contributing to the total signal at different levels: above the surface and at the sensor level in the middle wave and long wave infrared domains (i.e., from 3 to 14 µm). A phenomenological study is then conducted (§3) through simulations over two different types of natural homogeneous landscape (flat and rugged) and an heterogeneous urban case. Through these two first cases, an evaluation of the different contributors in the total signal is given at different wavelengths. The last case represents a

#8507 - $15.00 USD Received 18 August 2005; revised 27 February 2006; accepted 3 March 2006

more realistic configuration. It demonstrates the increasing impact of environment when enclosed spaces are in play.

2. Physical model

2.1. Model description

The spectral domain of concern is 3-14µm. For the seek of conciseness, the wavelength reference will not appear in equations. The studied relief is assumed to be composed of opaque materials. Each surface element is characterised by its spectral bidirectional reflectance, and its temperature. The radiance seen by the sensor is then Fig. 1:

$$L^{v} = \iint_{\Omega_{IFOV}} [\, L^{BOA}(P_{d\omega}) . t^{\uparrow}_{P_{d\omega}} + L^{atm,\uparrow}]\, d\omega \qquad (1)$$

where L^{v} is the radiance seen by the sensor inside its instantaneous field of view Ω_{IFOV}, L^{BOA} is the "Bottom Of Atmosphere" radiance, dω is an elementary solid angle such as $\iint_{\Omega_{IFOV}} d\omega = \Omega_{IFOV}$, $t^{\uparrow}_{P_{d\omega}}$ is the upwelling atmospheric transmission between the surface seen in the dω solid angle ($P_{d\omega}$) and the sensor, and $L^{atm,\uparrow}$ is the upwelling atmosphere radiance included in this solid angle.

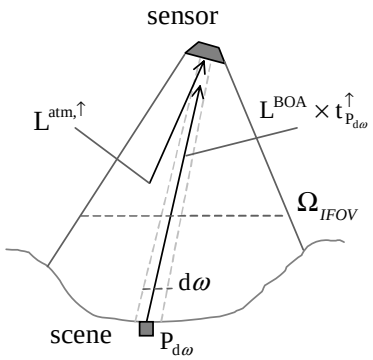

Fig. 1. Radiance seen by the sensor

The L^{BOA} radiance is composed of four terms Fig. 2:

$$L^{BOA}(P) = L_D(P) + L_A(P) + L_{emis}(P) + L_{env}(P) \qquad (2)$$

where
- $L_D(P)$ is the radiance coming from reflection of solar irradiance on P
- $L_A(P)$ is the radiance coming from reflection of atmospheric irradiance on P
- $L_{emis}(P)$ is the radiance coming from emission of the surface on P
- $L_{env}(P)$ is the radiance coming from reflection of environmental irradiance on P

The “solar” radiance is written Fig. 2 as:

$$L_D(P) = E_D(P) . \frac{\rho^{dd}_P(\overrightarrow{u_{sun}}, \overrightarrow{u_v})}{\pi} \qquad (3)$$

#8507 - $15.00 USD Received 18 August 2005; revised 27 February 2006; accepted 3 March 2006

where ρ_P^{dd} is the bidirectional reflectance at P, $\overrightarrow{u_{sun}}$ is the unit vector of the solar incidence, and $\overrightarrow{u_v}$ is the unit vector in the sensor direction at P. $E_D(P)$ is the solar irradiance at P :

$$E_D(P) = E_{TOA} . t^{\downarrow}(\overrightarrow{u_{sun}}, P).\left\langle \overrightarrow{n_P}. \overrightarrow{u_{sun}} \right\rangle .o(P) \qquad (4)$$

where E_{TOA} is the solar irradiance at the Top Of the Atmosphere, $t^{\downarrow}(\overrightarrow{u_{sun}}, P)$ is the downwelling transmission from the upper part of the atmosphere to P in the $\overrightarrow{u_{sun}}$ direction. $\overrightarrow{n_P}$ is a unit vector orthogonal to the surface at P. o(P) is the shade function which is set to 1 if P sees the sun or set to 0 if not.

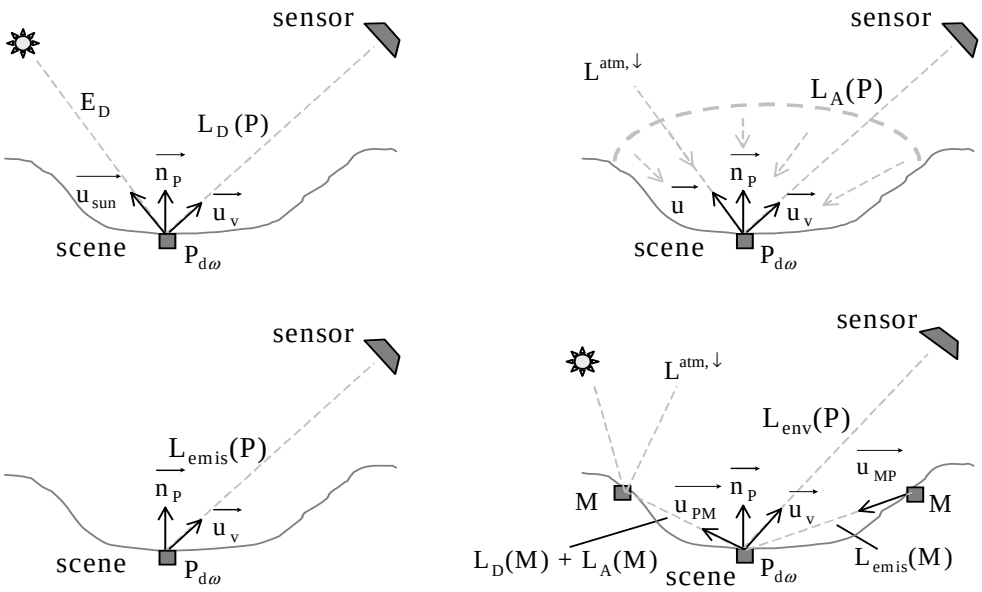

Fig. 2. Radiance contributors at BOA level

The "atmospheric" radiance is written as Fig. 2.

$$L_A(P) = \iint_{\Omega_{sky}} L^{atm,\downarrow}(\vec{u}; z_P).\left\langle \overrightarrow{n_P}.\overrightarrow{u} \right\rangle .\frac{\rho_P^{dd}(\vec{u}, \overrightarrow{u_v})}{\pi}.d\omega$$

$$+ \iint_{\overline{\Omega_{sky}}} L_{relief}^{atm,\downarrow}(\vec{u}; z_P).\left\langle \overrightarrow{n_P}.\overrightarrow{u} \right\rangle .\frac{\rho_P^{dd}(\vec{u}, \overrightarrow{u_v})}{\pi}.d\omega \qquad (5)$$

where Ω_{sky} is the solid angle where sky can be seen without obstacle. $L^{atm,\downarrow}$ is the downwelling atmospheric radiance in the direction $\overrightarrow{u}$, associated with the elementary solid angle dω. z_P is the height of P. $\overline{\Omega_{sky}}$ is the solid angle complementary to Ω_{sky} with regard to the

#8507 - $15.00 USD Received 18 August 2005; revised 27 February 2006; accepted 3 March 2006

hemisphere at P Fig. 3. $L_{relief}^{atm,\downarrow}$ is the downwelling atmospheric radiance in the direction $\vec{u}$ inside $\overline{\Omega_{sky}}$, meaning that only the part of the atmosphere located between the relief and P in that direction will contribute to this term. The split in the integral is introduced to highlight the difference in calculations when the portion of atmosphere is seen without obstacle and when the portion of atmosphere is included between the surface and the surrounding environment.

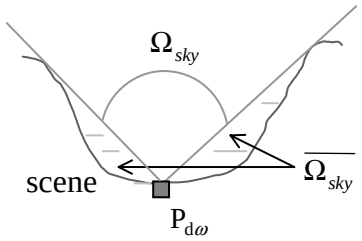

Fig. 3. Sky viewing solid angle

The "emission" radiance of the surface is written as Fig. 2:

$$L_{emis}(P) = \varepsilon_P(\vec{u_v}).L_{CN}(T_P) \tag{6}$$

where ε_P and T_P are respectively the emission and temperature at P. L_{CN} is the blackbody radiance.

The "environmental" radiance is expressed as Fig. 2:

$$L_{env}(P) = L_{D-env}(P) + L_{A-env}(P) + L_{emis-env}(P) \tag{7}$$

where $L_{D\text{-}env}$ is the radiance coming from reflection of direct solar irradiance reflected towards P by the neighbourhood, $L_{A\text{-}env}$ is the radiance coming from reflection of atmospheric irradiance reflected towards P by the neighbourhood and $L_{emis\text{-}env}$ is the radiance coming from emission from the neighbourhood towards P. Regarding environment, only single scattering is considered because in most cases it is sufficient excepted for very strong specular conditions. These terms are written as:

$$L_{D\text{-}env}(P) = \iint_{V(P)} \frac{\rho_P^{dd}(\vec{u}_{PM},\vec{u}_v)}{\pi}.E_D(M).\frac{\rho_M^{dd}(\vec{u}_S,\vec{u}_{MP})}{\pi}.t_{MP}.g_{MP}.dS_M \tag{8}$$

$$L_{A\text{-}env}(P) = \iint_{V(P)} \frac{\rho_P^{dd}(\vec{u}_{PM},\vec{u}_v)}{\pi}.\frac{E_{atm\_diffus}(M)}{\pi}.\rho_M^{dh}(\vec{u}_{MP}).t_{MP}.g_{MP}.dS_M \tag{9}$$

$$L_{emis\text{-}env}(P) = \iint_{V(P)} \frac{\rho_P^{dd}(\vec{u}_{PM},\vec{u}_v)}{\pi}.\varepsilon_M(\vec{u}_{MP}).L_{CN}(T_M).t_{MP}.g_{MP}.dS_M \tag{10}$$

where V is the neighbourhood of P, where M describes a facet in the neighbourhood. t_{MP} is the transmission between M and P. g_{MP} is a geometrical factor, taking into account the visibility and the distance between P and M, and the scalar products between the normal vectors of

#8507 - $15.00 USD Received 18 August 2005; revised 27 February 2006; accepted 3 March 2006

these facets $\left\langle \overrightarrow{n_P}.\overrightarrow{u_{PM}} \right\rangle$ and the viewing direction vectors $\left\langle \overrightarrow{n_M}.\overrightarrow{u_{MP}} \right\rangle$: $g_{MP} = \frac{\left\langle \overrightarrow{n_P}.\overrightarrow{u_{PM}} \right\rangle \left\langle \overrightarrow{n_M}.\overrightarrow{u_{MP}} \right\rangle}{r^2} v(M,P)$, where ν is a function of visibility between P and M. If P and M see each other ν = 1, else ν = 0. dS_M is the surface element in M. ρ_M^{dh} is the directional hemispherical reflectance at M. $E_{atm\_diffus}(M)$ stands for the part of atmospheric irradiance received in M, namely :

$$E_{atm\_diffus}(M) = \iint_{\Omega_{sky}} L^{atm,\downarrow}(\vec{u};z_M).\left\langle \overrightarrow{n_M}.\overrightarrow{u} \right\rangle.d\omega + \iint_{\Omega_{sky}} L^{atm,\downarrow}_{relief}(\vec{u};z_M).\left\langle \overrightarrow{n_M}.\overrightarrow{u} \right\rangle.d\omega \qquad (11)$$

2.2. Model implementation

The considered surfaces are heterogeneous and rugged. Triangular facets are the base of the geometric surface modelling which allows to reproduce complex scenes. Each facet is considered as homogeneous in optical properties and temperature. The radiative computations are performed in the centre of facets. Atmosphere is considered invariant along horizontal directions, hence it only depends on height z. Details of the day of the year, atmospheric conditions, geographical location and height of the site are given to Modtran [9] as inputs in order to obtain basic irradiances, radiances and transmissions in a flat homogeneous case: namely $L^{atm,\uparrow}$, E_{TOA}, $L^{atm,\downarrow}$, $L^{atm,\downarrow}_{relief}$, $t^{\uparrow}_{P\,d\omega}$, $t^{\downarrow}(\overrightarrow{u_{sun}},P)$ and t_{MP}. Transmissions are obtained directly from the Modtran ouput files using the transmission mode. E_{TOA} is also obtained directly from the Modtran ouput files using the solar irradiance mode. Radiances are obtained directly from the Modtran ouput files using the radiance mode. In order to obtain $L^{atm,\uparrow}$ one run is enough while for $L^{atm,\downarrow}$ and $L^{atm,\downarrow}_{relief}$ a run is necessary for each viewing direction $\overrightarrow{u}$, associated with the elementary solid angle dω. These components are then used in the previously described equations that account for the relief. When comparing with Modtran for flat surfaces, this model implementation induces negligeable errors in the calculation in LWIR ($<10^{-3}$ %) and small ones in MWIR (~3%) due partly to splitting up the sun-ground-sensor path and partly to introducing a step important (10° in θ and 20° in φ) in the sky solid viewing angle integration. However, when rugged surfaces are in play, Modtran can not be used directly to derive $E_D(P)$ or $L_A(P)$ and using a smaller step will induce an important computation cost.

The global environment is composed of a repetition of the initial pattern with the same properties, irradiances and radiances. The size of environment that has to be considered depends on the relief size. Typically, when considering a weakly rugged surface which lengths a few hundred meters, taking an environment of the same length or twice this length is sufficient, but an open almost flat scene surrounded by mountains may require a larger environment. In fact, it consists of attaining the surrounding environment. For enclosed spaces like urban environment, a reduced area (tens of meters) will describe environment fairly enough. In addition, the digitization of the scene has to be chosen regarding the homogeneity scale of the scene and the observation resolution. In the model, there is no technical restriction in this choice, except memory requirements.

3. Simulation results and analysis

3.1. Introduction

This paragraph aims to illustrate and highlight the impact of radiative effects in 3D landscapes. To fulfil this goal, two typical landscapes are considered. They are compared to the corresponding flat surfaces (i.e. composed of the same materials with the same

#8507 - $15.00 USD Received 18 August 2005; revised 27 February 2006; accepted 3 March 2006

temperatures). The selected scenes represent respectively a sand hill Fig. 4(a) and a simple urban area Fig. 4(b). Both profiles are invariant along the transversal direction (i.e. orthogonal to the profiles).

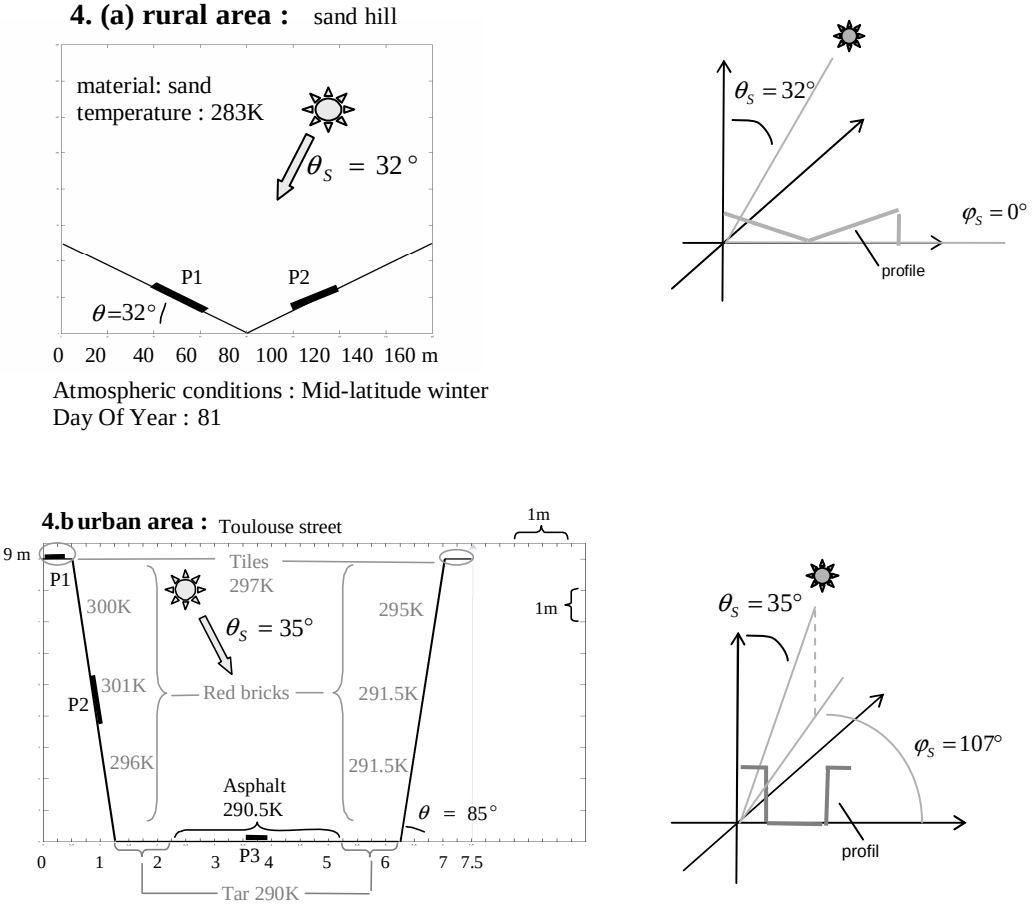

Fig. 4. Simulated cases

The sand hill is homogeneous in material and temperature. Its spectral reflectance (extracted from the database ASTER [12]) is plotted on Fig. 5(a). The spectral emissivities are deduced from the spectral reflectances considering the lambertian assumption. Its temperature is set to 10°C over the profile. The solar plane belongs to the same plane the profile is, and its incidence zenith angle on the surface is set to 32°.

#8507 - $15.00 USD Received 18 August 2005; revised 27 February 2006; accepted 3 March 2006

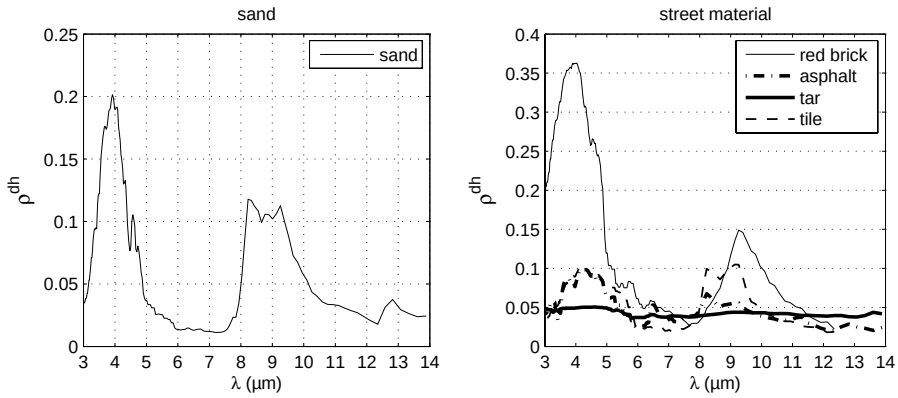

Fig. 5 (a) sand reflectance (sand hill case) (b) street materials reflectances (urban case)

The urban area is made of different typical materials [Fig. 4(b)] which spectral reflectances (also taken from ASTER [12]) are plotted on Fig. 5(b). It is composed of red brick walls circling a pavement made of tar (sidewalks) and of asphalt (road). The roofs of the two buildings represented are made of terra cotta tiles. The temperature of each material is set according to the measurements taken during the Capitoul campaign in Toulouse, France [7]. The sun azimuth angle is off the profile plane (107°), and the incidence zenith angle is 35°. The profile plane is located 135° off the North. As the digitalisation of the relief is performed with a regular grid, it is not possible to model vertical walls. Hence, they are approximated with quasi-vertical facets (with an 85° slope). However, this drawback does not bring significant changes on the results.

The different simulations consist in nadir viewing acquisitions from a 2km's high airborne sensor. For the desert case, spectral radiances are simulated with the standard mid-latitude winter type with a standard rural aerosol type (10km's visibility). For the urban case, the atmospheric profile used is the standard mid-latitude summer type. The same respective conditions are used to simulate the corresponding flat cases: rural (sand) and urban. As a first step, the spectral radiances for the flat and rugged cases are shown for the usual atmospheric windows 3-5µm (Middle Wave InfraRed: MWIR) and 8-14µm (Long Wave InfraRed: LWIR). However, when detailed analyses of the signal are presented, we focused on four specific wavelengths representative of the main phenomena involved: 3.9µm, 4.7µm, 8.6µm and 11µm. As our model is a part of an end-to-end simulator under development, after the simulation of the spectral sensor radiance, the inverse process is required to retrieve the surface parameters: land surface temperature (LST) and spectral emissivity. Thus, an estimation of the accuracy on these retrieved surface parameters is conducted, assuming the atmospheric conditions perfectly known.

#8507 - $15.00 USD Received 18 August 2005; revised 27 February 2006; accepted 3 March 2006

3.2 Sand hill

Sensor radiance for the flat and the rugged cases is plotted against wavelength in Fig. 6.

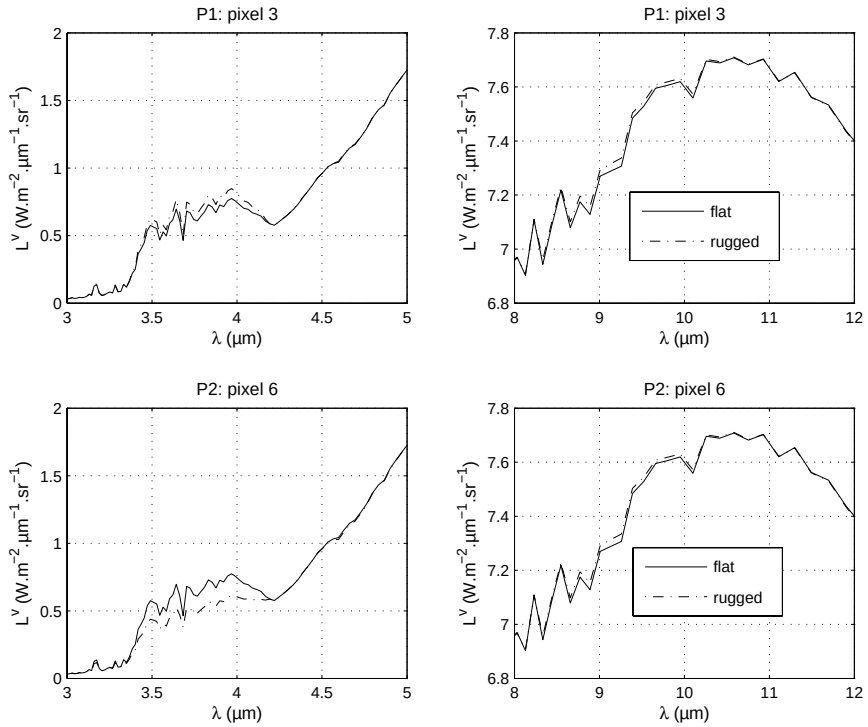

Fig. 6. Sensor radiance for the sand cases (flat and hill)

The presented radiances result from two facets P1 and P2 representative of each side of the rugged scene in Fig. 4(a). The relative difference between the two signals (i.e. $\frac{L^{v}_{rugged} - L^{v}_{flat}}{L^{v}_{flat}} * 100$) is then plotted in Fig. 7 for the four wavelengths of interest against the localisation of each facet on the surface. The results show that a flat surface radiative transfer code underestimates the signal over sunlit areas and overestimates it over less sunlit or shadowed areas. The main difference appears in the MWIR domain. At 3.9μm, it reaches +10% for the left slope of the sand hill, which is the most sunlit and -22% on the opposite part. For the other wavelengths, the difference is less than 1%.

#8507 - $15.00 USD Received 18 August 2005; revised 27 February 2006; accepted 3 March 2006

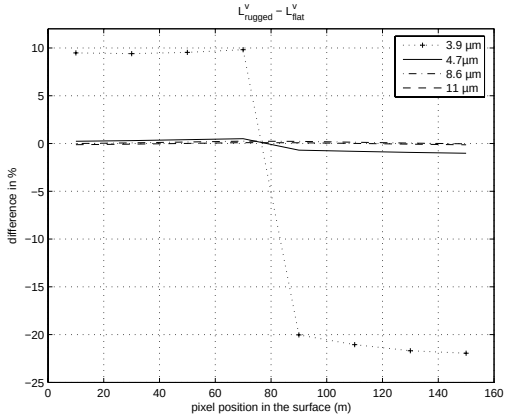

Fig. 7. Relative difference between flat and rugged surfaces (hill case)

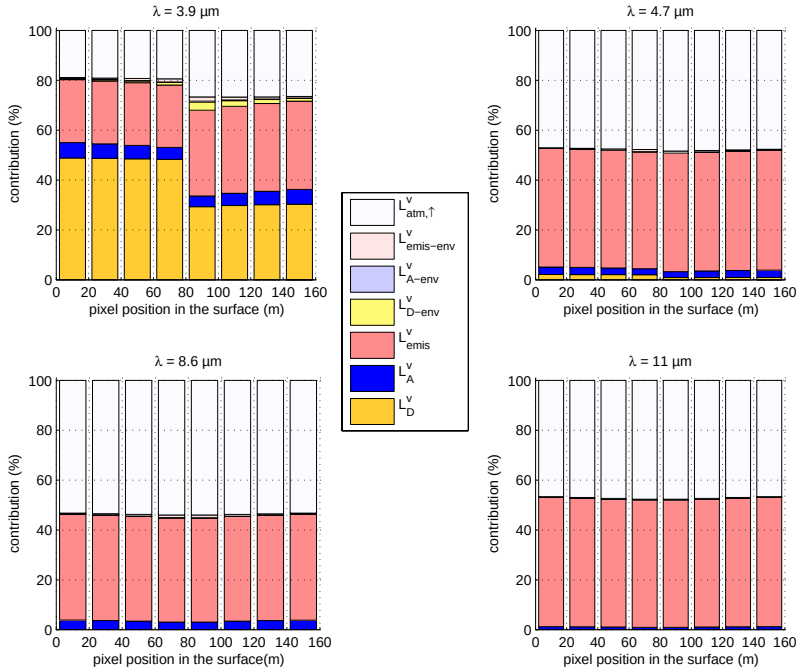

Fig. 8. Relative contribution of each sensor radiance component for the sand hill case

Figure 8 presents the composition of the sensor signal against the position of each facet on the sand hill surface. This allows to evaluate the relative contribution of each component at the sensor level. As a comparison, the same representation is given for the flat case in Fig. 9. At 4.7, 8.6 and 11µm, the proportion of each component in the total signal does not vary significantly along the profile. Moreover, it is almost not affected by slopes. The solar incident irradiance is low, as is the environment contribution. In addition, as the sand reflectance values are small, the main phenomena contributing to the sensor radiance is emission, which does not depend on the geometry of the surface. Hence the relief impact is weak. On the contrary, at 3.9 µm the reflected solar beam contributes up to half of the sensor radiance. The slope effects then rise in the signal. Plus, as the sand reflectance value is higher at 3.9µm, the adjacency components L^v_{*-env} reach up to 5% of the sensor signal. This

#8507 - $15.00 USD Received 18 August 2005; revised 27 February 2006; accepted 3 March 2006

component varies from one side of the hill to the other side because sunlit is stronger on the first side of the hill.
The environment component amount rises as approaching the bottom of the hill because the geometrical factor g_{MP} , Eq. (8)-(10), is higher.

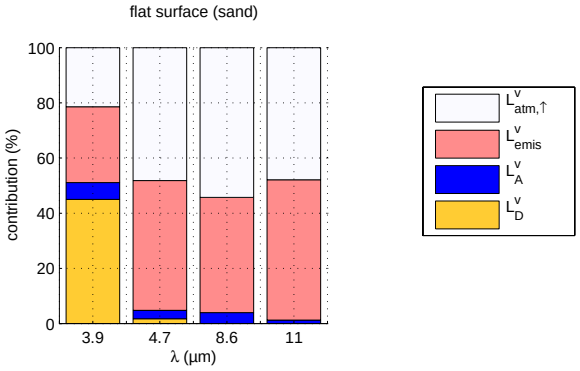

Fig. 9. Relative contribution of each sensor radiance component for the sand flat case

As a result, when considering ground surface emissivity extraction from remote sensing, neglecting the relief can introduce error between 3 and 4μm. In order to evaluate it in the present case, the spectral BOA radiance (which is usually deduced after atmospheric corrections) is analysed on Fig. 10 and Fig. 11.

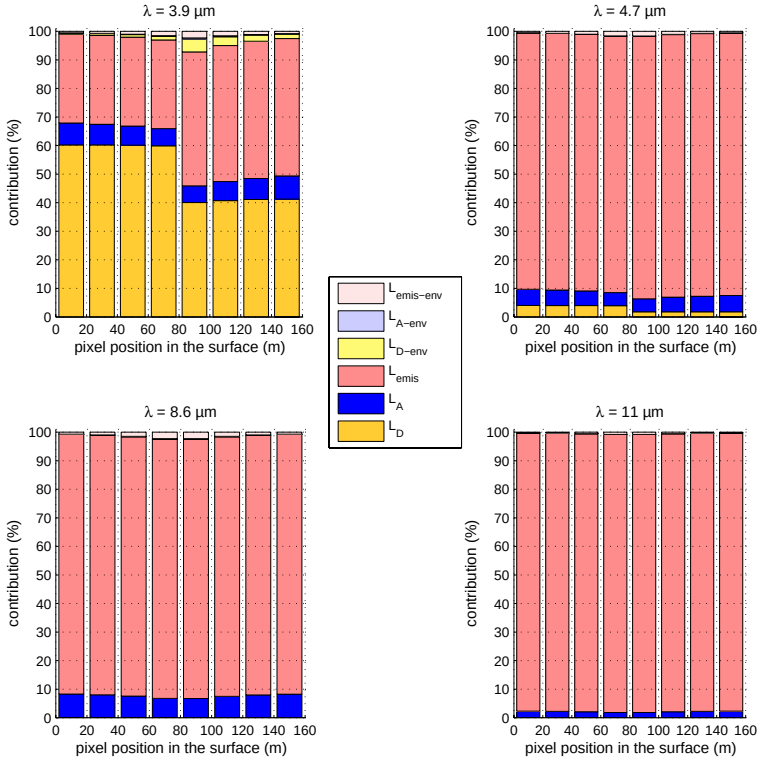

Fig. 10. Relative contribution of each BOA radiance component for the sand hill case

#8507 - $15.00 USD Received 18 August 2005; revised 27 February 2006; accepted 3 March 2006

At ground level, the relative contribution of the environment components increases, larger as the wavelength decreases. As a result, at 3.9µm the total adjacency components weight more than 7% of the hill case signal. The rise of this quantity comes from the suppression of the upward radiance (since it is BOA signal), which was the third term of importance in the sensor signal. This leads to a rise of each component contribution: in the most sunlit side at 3.9µm, the solar contribution gains 12%, the atmospheric contribution gains 2% . At 8.6µm, the emission contribution gains 48%. The importance of a good description of every term is then emphasised in the study of the BOA signal. This fine description can be found in Fig. 11. A detailed analysis of the discrepancy factors of the signal is presented for each term at 3.9µm. We focused on this wavelength because reflection phenomena are the most dependent on the relief. In the LWIR, the dominant phenomenon being the emissivity which does not depend on the relief, less differences are found. At 3.9µm, behaviour discrepancy along the profile is easier to highlight.

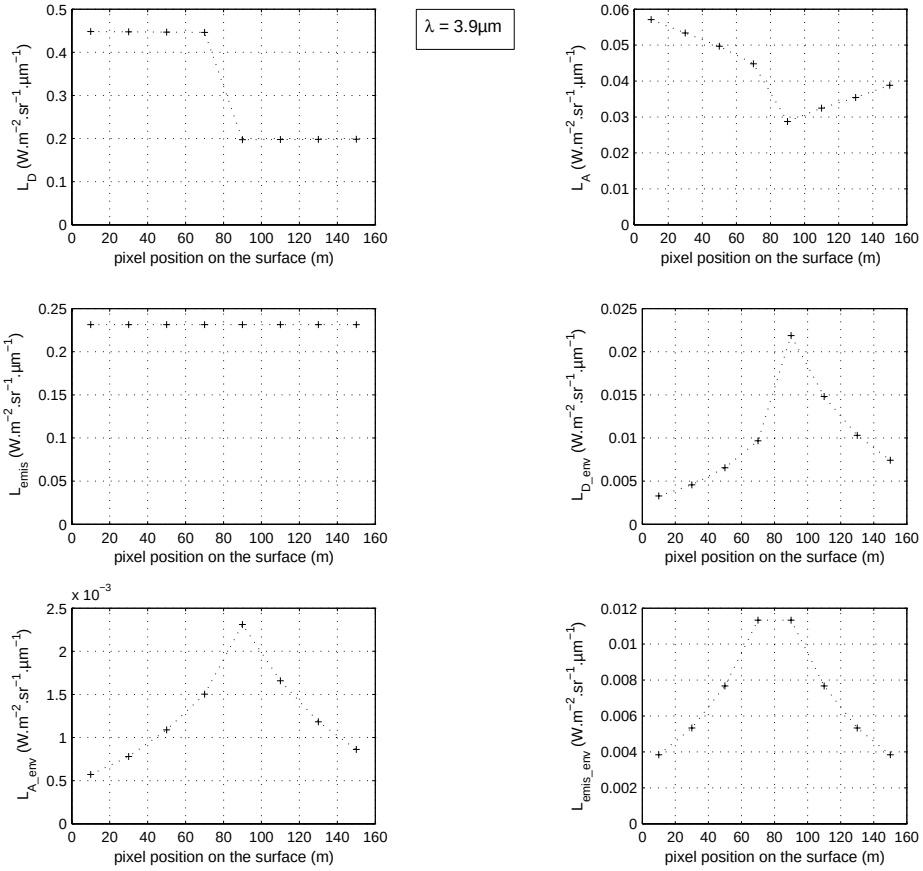

Fig. 11. LBOA terms against facet location in the surface for the sand hill case at 3.9µm

• $L_{\mathrm{D}}^{\mathrm{BOA}}$: this term depends of course on illumination conditions. But it depends also on the surface height, the slope of the surface, and environment. Shade and environment induced shade is taken into account in our model, as shade nullifies the $L_{\mathrm{D}}^{\mathrm{BOA}}$ term. The shade of a facet is calculated given incidence zenithal angle of the sun, orientation of the facet and shade induced by the neighbourhood. If the facet is shaded, then $L_{\mathrm{D}}^{\mathrm{BOA}}$ is zero. The slope of the surface implies that irradiance is multiplied by the cosine of the incidence angle on the

#8507 - $15.00 USD Received 18 August 2005; revised 27 February 2006; accepted 3 March 2006

surface, which means important variations of the irradiance value depending on the surface slope are to be found. The slant variation of the slope (-32°/+32°) induces a variation that diminishes this term value by two (0.45/0.2W.m^{-2}.µm^{-1}.sr^{-1}). If a flat hypothesis was taken for that case, this variation could have led to misinterpret it as a variation due to an reflectance variation, and thus to a misinterpretation of the scene composition. Last, the higher the surface is, the lesser atmosphere is crossed, and then solar irradiance is stronger. For our case, this effect is weak and hardly visible at the scale of the figure since only a 50metres'depth is used.

• $L_{\mathrm{A}}^{\mathrm{BOA}}$: this term depends also on geographical and day-time position, and wavelength. But it depends mostly on the orientation of the surface and its environment. As explained in the theoretical part, the sky view solid angle is the most important influence parameter for this term. The sky view solid angle determines the portion of irradiance irradiating the surface. But the part of the atmosphere seen is important as well. In a horizontal long path, more particles are seen than in a vertical long path. Therefore a solid angle looking nadir will intercept less radiance than a solid angle looking off-nadir. At 3.9µm, we notice an asymmetrical curve, due to the aerosol front scattering.

• $L_{\mathrm{emis}}^{\mathrm{BOA}}$: in our case, emissivity depends only on wavelength as a lambertien value is used for the simulation cases. It is therefore the same value for both sides of the hill.

• $L_{\mathrm{D\text{-}env}}^{\mathrm{BOA}}$, $L_{\mathrm{A\text{-}env}}^{\mathrm{BOA}}$ and $L_{\mathrm{emis\text{-}env}}^{\mathrm{BOA}}$: our neighbourhood is represented by a 200m square around each facet. These three terms depend on the direct terms and the geometrical factor g_{MP}. This factor is function of the geometry of the surface only. Its form can be directly observed in the $L_{\mathrm{emis\text{-}env}}^{\mathrm{BOA}}$ curve as $L_{\mathrm{emis}}^{\mathrm{BOA}}$ is the same for every neighbour. At 3.9µm, $L_{\mathrm{D\text{-}env}}^{\mathrm{BOA}}$ and $L_{\mathrm{A\text{-}env}}^{\mathrm{BOA}}$ present a dissymetry between the two slopes of the hill. This is a consequence of the asymmetry of the direct curves $L_{\mathrm{D}}^{\mathrm{BOA}}$ and $L_{\mathrm{A}}^{\mathrm{BOA}}$. As environment is in play, this asymmetry is inverted and the right side of the hill receives more irradiance than the left side. This dissymetry disappears in the LWIR because the solar effects disappear. Each term analysis helps either to uncover information or to tally with previous information from other terms.

In order to have a proper evaluation of the error done on the emissivity retrieval, the starting point is the BOA radiance. For a flat scene, the BOA radiance is commonly expressed as (Malaplate et al. [13]):

$$\begin{aligned} \mathrm{L}^{\mathrm{BOA}} &= \mathrm{L}_{\mathrm{D}}(\mathrm{P}) + \mathrm{L}_{\mathrm{A}}(\mathrm{P}) + \mathrm{L}_{\mathrm{emis}}(\mathrm{P}) \\ &= (1-\varepsilon)\frac{\mathrm{E}_{\mathrm{D}}(\mathrm{P})}{\pi} + (1-\varepsilon)\mathrm{L}^{\mathrm{atm},\downarrow} + \varepsilon\ \mathrm{L}_{\mathrm{CN}}(\mathrm{T}) \end{aligned} \tag{12}$$

Usually, temperature is derived using LWIR bands. If temperature is retrieved correctly and atmospheric parameters are evaluated without errors, the error on emissivity is then deduced from Eq. (12):

$$\begin{aligned} \Delta\mathrm{L}_{\mathrm{BOA}} &= \Delta[(1-\varepsilon)\frac{\mathrm{E}_{\mathrm{D}}(\mathrm{P})}{\pi} + (1-\varepsilon)\mathrm{L}^{\mathrm{atm},\downarrow} + \varepsilon\ \mathrm{L}_{\mathrm{CN}}(\mathrm{T})] \\ &= \Delta[(1-\varepsilon)\frac{\mathrm{E}_{\mathrm{D}}(\mathrm{P})}{\pi}] + \Delta[(1-\varepsilon)\mathrm{L}^{\mathrm{atm},\downarrow}] + \Delta[\varepsilon\ \mathrm{L}_{\mathrm{CN}}(\mathrm{T})] \\ &= -\Delta\varepsilon\frac{\mathrm{E}_{\mathrm{D}}(\mathrm{P})}{\pi} - \Delta\varepsilon\ \mathrm{L}^{\mathrm{atm},\downarrow} + \Delta\varepsilon\ \mathrm{L}_{\mathrm{CN}}(\mathrm{T}) \end{aligned}$$

#8507 - $15.00 USD Received 18 August 2005; revised 27 February 2006; accepted 3 March 2006

as $\Delta \frac{E_D(P)}{\pi} = \Delta L^{atm,\downarrow} = \Delta L_{CN}(T) = 0$.

Then

$$\Delta\varepsilon = \frac{\Delta L_{BOA}}{[L_{CN}(T) - L^{atm,\downarrow} - \frac{E_D(P)}{\pi}]} \quad (13)$$

The error on emissivity is calculated introducing an error in the L_{BOA} calculation, namely an error that could be done considering flat a rugged surface. For instance, considering flat the sand hill case, a bias on L_{BOA} produced by the relief and the adjacency components of 10% introduces then a significant error on the retrieved emissivity of more than 11% at 3.9µm (see table 1). This error is maximum on the right side of the hill because, as we explained earlier, environment effects are stronger on this side. This error is linked to the environmental contribution. In LWIR, environment effects are weaker but remain important. The error reduces to less than 1% at 11µm and 2.6% at 8.6µm, where the reflectance has a higher level due to the restrahlen effect.

Table 1. Absolute measure uncertainty over a sand hill case using the flat hypothesis .

	west side: facet 1				East side: facet 2			
	3.9µm	4.7µm	8.6 µm	11µm	3.9µm	4.7µm	8.6 µm	11µm
$\Delta\varepsilon$	-0.0435	-0.042	0.0234	0.0065	0.0938	0.0183	0.021	0.0063
$\frac{\Delta\varepsilon}{\varepsilon}\%$	-5.43	-4.54	2.63	0.67	11.71	2.	2.36	0.65

3.3 Urban area

Urban surfaces development leads to a growing interest. Hence Land Surface Temperature (LST) is one of the key parameter controlling the urban climatology [6]. Surface and atmospheric modifications due to urbanisation generally lead to a change of thermal flux between urban area and the surrounding rural area. Such landscape has a very complex 3D structure which introduces directional effects [8] at the sensor level and cavity effects [13]. In order to highlight the importance of these phenomena, we applied our model to a city case. It brings a first evaluation of the sensor signal over the city, which is compared to the corresponding flat surface (same composition but without relief). We will also evaluate the error done on temperature and emissivity by using a flat surface hypothesis.

To conduct the analysis over the street case, three facets locations in the profile were chosen [see Fig. 4(b)]. The first one (P1) is located on the roof. The second one (P2) is located on the wall, and the third one (P3) is located on the ground in the middle of the street. The corresponding sensor radiance is then plotted against the wavelength for each facet in Fig. 12. The sensor radiance is also plotted for the corresponding flat surface.

#8507 - $15.00 USD Received 18 August 2005; revised 27 February 2006; accepted 3 March 2006

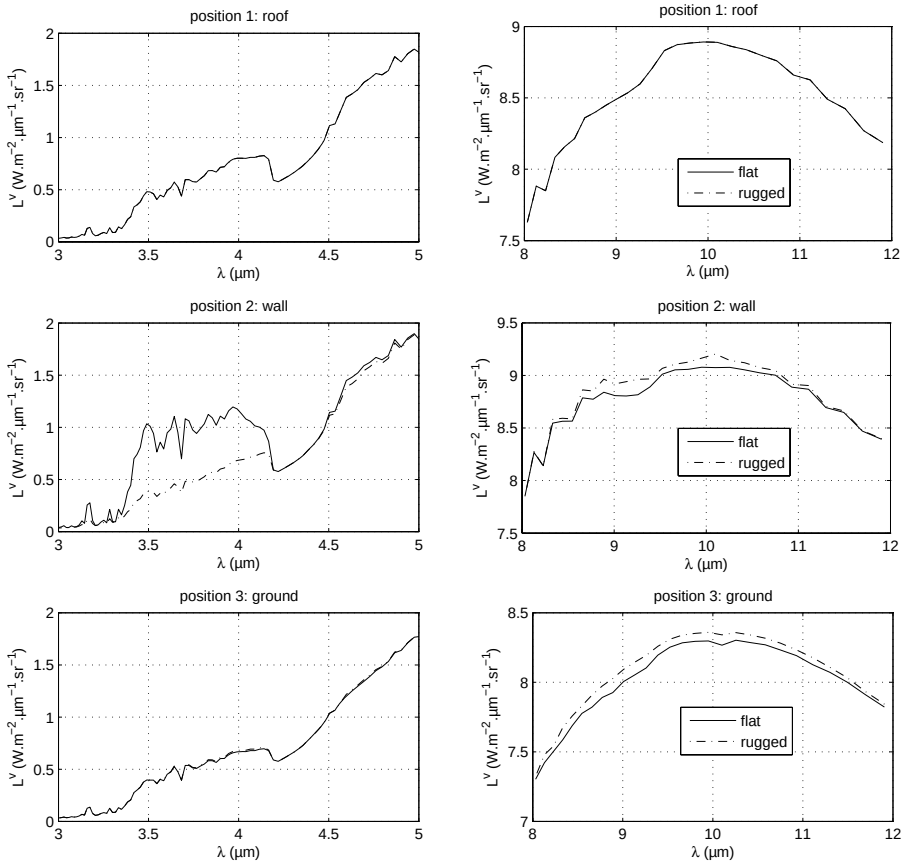

Fig. 12. Sensor radiance for flat and urban surfaces

On the roof (P1), environmental contribution is null. Hence the difference with the flat case is less than 1% in Fig. 13. For P2 and P3, environment is a term of importance so a strong difference appears. As for the sand hill case, the main difference appears in the MWIR for the facet located on the wall (P2). It now reaches 48% at 3.9μm and 4% at 4.7μm in Fig. 13, which is twice the value of the difference for the sand hill case. For P3, the error is less important (~2%) because ground reflectances (tar and asphalt) are low. The environment term is then also lower than for P2. For urban studies in the MWIR, the flat hypothesis leads to really important errors. In the LWIR, the difference is now approaching 1%, but is still weak due to the lower environment contribution.

#8507 - $15.00 USD Received 18 August 2005; revised 27 February 2006; accepted 3 March 2006

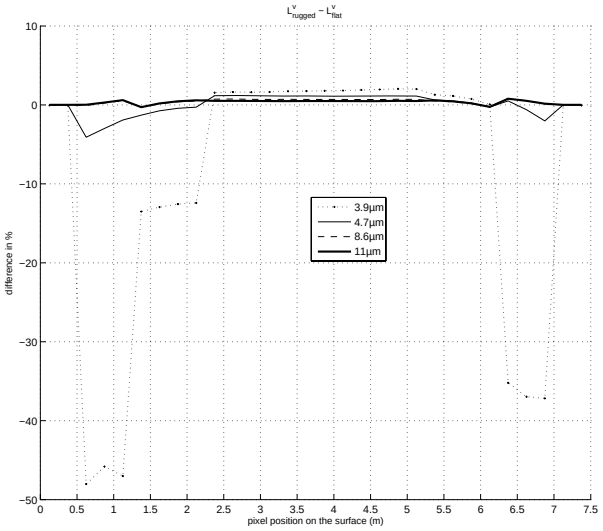

Fig. 13. Relative difference between flat and rugged surfaces (street case)

However, the difference is higher for the wall and ground position than for the roof because they receive irradiance due to emission from the neighbourhood. The link between the error done considering flat a rugged surface and the environment contribution is obvious when analysing the composition of the signal at the sensor level against the position of the facet seen in the street profile in Fig. 14.

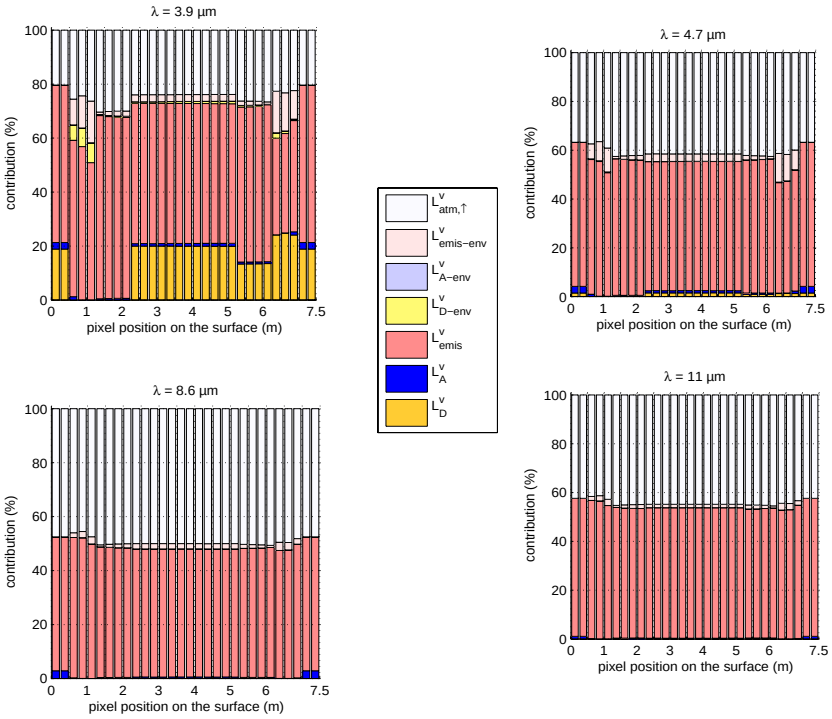

Fig. 14. Relative contribution of each sensor radiance component for the urban street case

#8507 - $15.00 USD Received 18 August 2005; revised 27 February 2006; accepted 3 March 2006

The environment component weight in the signal ranges now from 2.8% (11µm) to 22.8% (3.9µm) instead of 5% maximum in the sand case (3.9µm). To the contrary, the solar contribution diminishes in the street due to the change of materials. Its maximum value falls from 50% to 20%. Except for the tiles which reflectance is higher than the sand one, the other materials in the street have a lower reflectance. As an example, the sand reflectance value is twice the tile reflectance one at 3.9µm. This effect is more obvious for the corresponding flat surface Fig. 15 where only the material reflectances play a part in the percentage of the solar contribution in the signal. As the reflectances are lower, the emissivities are higher and then emission contribution is stronger in the urban case.

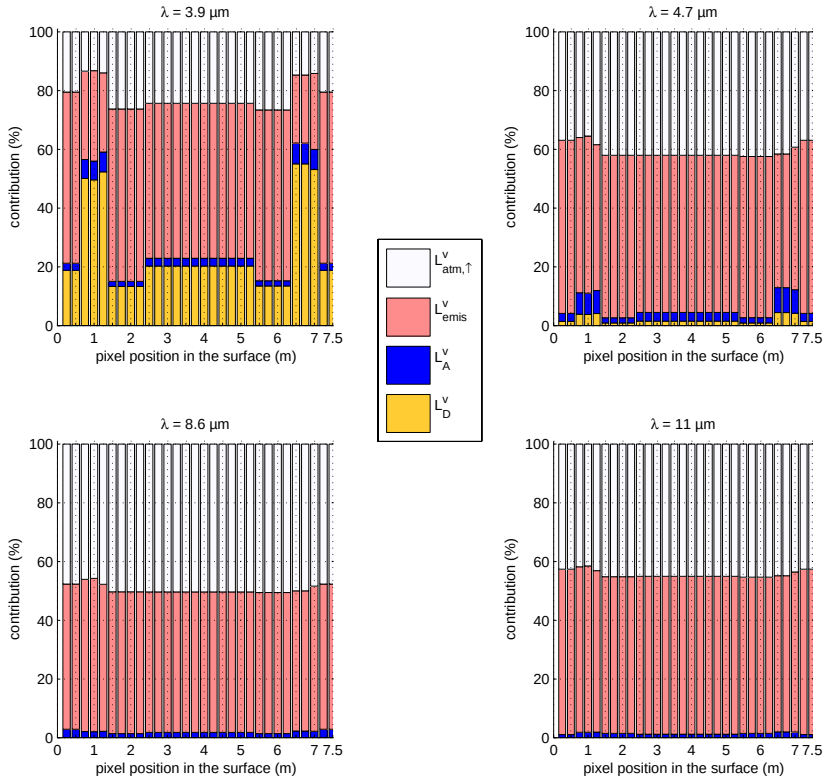

Fig. 15. Relative contribution of each sensor radiance component for the urban flat case

In addition, higher temperatures were considered in the urban case. Therefore, emission is the dominant contribution from far: 60% for the street case while ~30% for the sand hill case at 3.9µm (as the hill was fully sunlit, only sunlit facet are compared). In the BOA signal in Fig. 16, the environment contribution rises too and ranges from 31% (3.9µm) to 6% (8.6µm). Therefore this contribution is not negligible anymore. This impacts the signal and rises the difference when comparing with the flat signal. This is mainly due to increased adjacency effects. First, the distance between the facets reduces: in the sand hill case, the nearest facets that can interact are distant by 20m, meanwhile in the street case, they are distant by 1.5m. Second, the slant of wall rises compared to the hill case, which raises the roughness.

#8507 - $15.00 USD Received 18 August 2005; revised 27 February 2006; accepted 3 March 2006

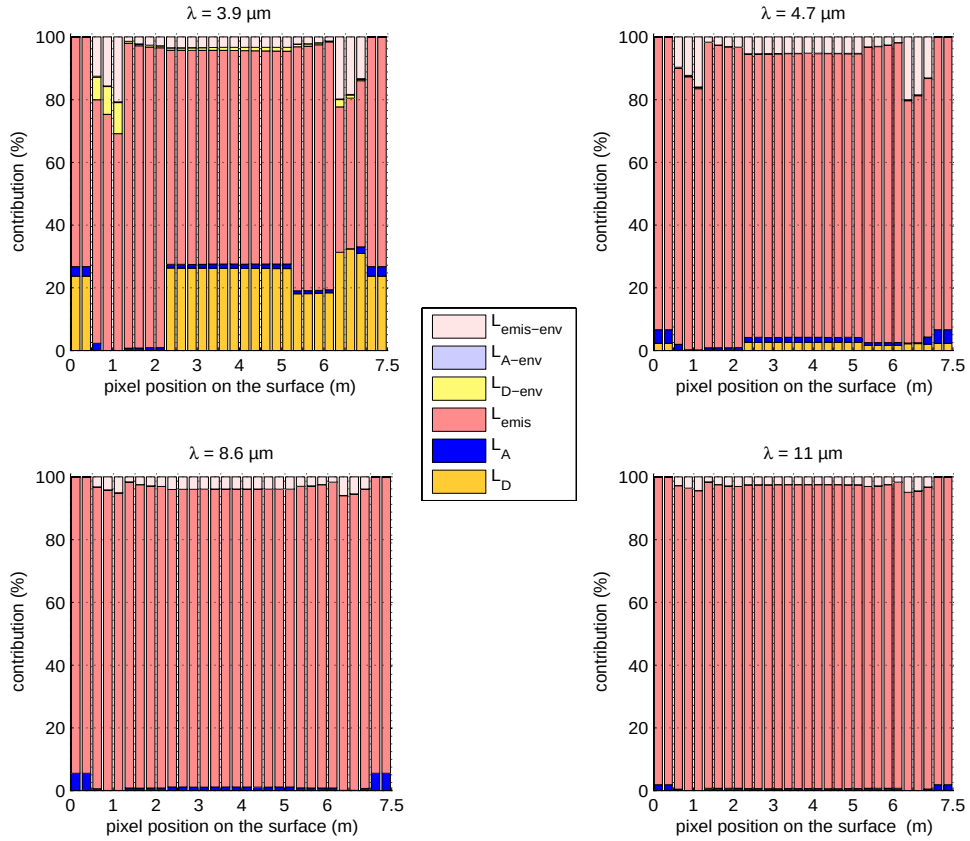

Fig. 16. Relative contribution of each BOA radiance component for the urban street case

#8507 - $15.00 USD Received 18 August 2005; revised 27 February 2006; accepted 3 March 2006

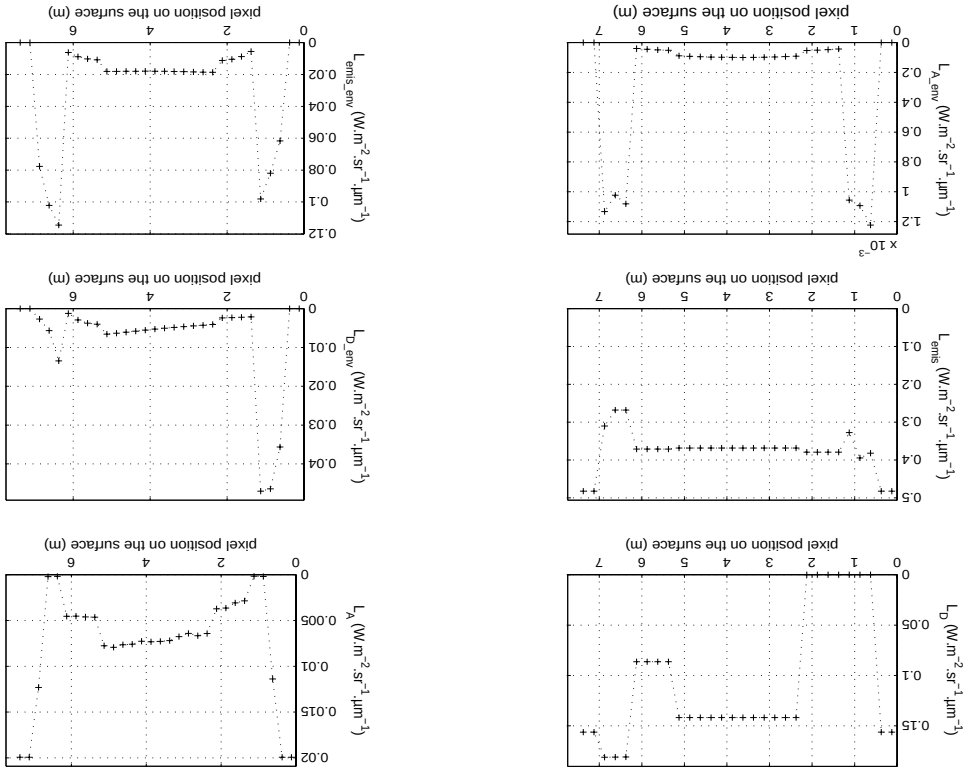

Fig. 17. LBOA terms against facet location in the surface for the urban street case at 3.9µm

The interest of having a fine description of each term of the BOA signal in Fig. 17 is obvious in urban cases. As a matter of fact, as the scene is heterogeneous and rugged, it is difficult to separate effects from heterogeneity from effects due to roughness. The access to the set of graphs removes this uncertainty. Roughness is detected through the shadow effects in the $L_{\mathrm{D}}^{\mathrm{BOA}}$ graph, and the sky viewing angle influence in the $L_{\mathrm{A}}^{\mathrm{BOA}}$ graph. Obviously, it appears too in the graphs for the environment terms. Heterogeneity can be spotted in the $L_{\mathrm{emis}}^{\mathrm{BOA}}$ graph as this term does not depend on the relief.

When the error for retrieving parameters is evaluated in the street case, using Eq. (12) and (13), the uncertainty rises (table 2). The error done on the emissivity rises to 35% at 3.9µm when walls are considered. But walls are not often directly seen in airborne images. So the important places to evaluate error are in the grounds and in the roofs. At 3.9µm in the middle of the ground the error for emissivity reaches almost 6% at 3.9µm and 1.6% at 8.6µm.

If emissivity is retrieved correctly, than the error on the temperature is written as:

$$\Delta \mathrm{T} = \frac{\Delta \mathrm{L}^{\mathrm{BOA}}}{\varepsilon \dfrac{\partial \mathrm{L}_{\mathrm{CN}}(\mathrm{T})}{\partial \mathrm{T}}} \tag{14}$$

#8507 - $15.00 USD Received 18 August 2005; revised 27 February 2006; accepted 3 March 2006

Table 2. Absolute measure uncertainty over a street case using the flat hypothesis .

	Roof				Wall			
	3.9m	4.7µm	8.6 µm	11µm	3.9µm	4.7µm	8.6 µm	11µm
$\Delta\varepsilon$	0.0002	-0.0001	-0.0002	-0.0001	-0.3227	-0.0724	0.0042	0.005
$\frac{\Delta\varepsilon}{\varepsilon}\%$	0.026	-0.0097	-0.0181	-0.0072	-35.11	-9.58	0.45	0.53
ΔT	0.003	-0.002	-0.0067	-0.0042	-14.85	-0.97	0.19	0.29
$\frac{\Delta T}{T}\%$	0.01	<-0.001	-0.0023	-0.0014	-4.93	-0.32	0.06	0.1

	Ground			
	3.9µm	4.7µm	8.6 µm	11µm
$\Delta\varepsilon$	0.0553	0.0223	0.0152	0.0095
$\frac{\Delta\varepsilon}{\varepsilon}\%$	5.82	2.35	1.59	1
ΔT	0.96	0.71	0.97	0.74
$\frac{\Delta T}{T}\%$	0.23	0.18	0.23	0.19

The maximum error is encountered in the MWIR for temperature as well, but it still reaches 1K in the LWIR (8.6µm) for ground. This is induced by the rise of the importance of environmental terms.

4. Conclusion

A new radiative transfer model has been presented allowing to compute the sensor radiance over rugged heterogeneous simple landscapes in the 3-14µm domain. Unlike the other common radiative transfer codes, this new tool is able to take into account the 3D geometry of the studied areas and thus model the different new radiance components introduced by this structure. This code can estimate the different contributors of the signal at sensor and ground levels. This is a key point to develop appropriate retrieval algorithm to estimate the surface parameters. This point is particularly crucial for the high spatial resolution sensors in the infrared domain over complex scenes like urban areas.

To exhibit the potentiality of this code, two study cases have been presented: a sand hill and an urban case. For each case, a phenomenological study has been conducted at different levels and the uncertainty of the surface parameters retrieval has been estimated, showing the impact of the relief.

The sand hill case showed the construction of the sensor signal, and the importance of each term in the signal. Emissivity (coming from the surface and the atmosphere) is the first term of importance in MWIR and in LWIR, therefore it should be estimated with a good precision. Nevertheless, as the solar component is the second term of importance in MWIR, it has to be estimated as well. The impact of the relief shape on this term has been presented. The error of using a flat hypothesis and its effects on the emissivity term has been discussed. We have shown that it leads to over 10% error at 3.9µm, which will occur on the first term of importance. However, for such profile, the topographic effects are weaker in the LWIR.

#8507 - $15.00 USD Received 18 August 2005; revised 27 February 2006; accepted 3 March 2006

The urban case highlighted the difficulty to separate and recognise the different causes of discrepancy in the signal along the profile when heterogeneity concurs with roughness and a deep analysis is not conducted. It highlighted too the importance of environment contribution in complex surfaces as it reaches in the presented case over 20% of the total sensor signal at 3.9µm and 6% of the BOA signal at 8.6µm. This raise of the environment contribution leads to a rise of the incertitude done in the retrieval of surface properties. The error affecting the emissivity reaches in this case 6% at 3.9µm, and the error on the temperature is 1K at 8.6µm.

Further works are planned especially concerning experimental validation. Measurements were made during winter 2004-2005 within the CAPITOUL campaign [7] and are currently under analysis.

#8507 - $15.00 USD Received 18 August 2005; revised 27 February 2006; accepted 3 March 2006